



HAL
open science

Determination of Na⁺ Cation Locations in Nanozeolite ECR-1 Using a 3D ED Method

Taylan Örs, Irena Deroche, Corentin Chatelard, Mathias Dodin, Raquel Martinez-Franco, Alain Tuel, Jean-Louis Paillaud

► **To cite this version:**

Taylan Örs, Irena Deroche, Corentin Chatelard, Mathias Dodin, Raquel Martinez-Franco, et al.. Determination of Na⁺ Cation Locations in Nanozeolite ECR-1 Using a 3D ED Method. *Symmetry*, 2024, 16 (4), pp.477. 10.3390/sym16040477 . hal-04554569

HAL Id: hal-04554569

<https://hal.science/hal-04554569>

Submitted on 22 Apr 2024

HAL is a multi-disciplinary open access archive for the deposit and dissemination of scientific research documents, whether they are published or not. The documents may come from teaching and research institutions in France or abroad, or from public or private research centers.

L'archive ouverte pluridisciplinaire **HAL**, est destinée au dépôt et à la diffusion de documents scientifiques de niveau recherche, publiés ou non, émanant des établissements d'enseignement et de recherche français ou étrangers, des laboratoires publics ou privés.



symmetry



Article

Determination of Na⁺ Cation Locations in Nanozeolite ECR-1 Using a 3D ED Method

Taylan Örs, Irena Deroche, Corentin Chatelard, Mathias Dodin, Raquel Martinez-Franco, Alain Tuel and Jean-Louis Paillaud

Special Issue

Electron Diffraction and Structural Imaging II

Edited by


Dr. Partha Pratim Das, Dr. Arturo Ponce-Pedraza, Dr. Enrico Mugnaioli and Dr. Stavros Nicolopoulos



<https://doi.org/10.3390/sym16040477>

Article

Determination of Na⁺ Cation Locations in Nanozeolite ECR-1 Using a 3D ED Method

Taylan Örs^{1,2}, Irena Deroche^{1,2} , Corentin Chatelard^{3,4}, Mathias Dodin³, Raquel Martinez-Franco³, Alain Tuel⁴ and Jean-Louis Paillaud^{1,2,*}

¹ Institut de Science des Matériaux de Mulhouse (IS2M), UMR CNRS 7361, Université de Haute-Alsace, 15 Rue Jean Starcky, 68100 Mulhouse, France; taylan.ors@uha.fr (T.Ö.); irena.deroche@uha.fr (I.D.)

² Université de Strasbourg, 67000 Strasbourg, France

³ IFP Energies Nouvelles-Etablissement de Lyon, Rond-Point de l'Échangeur de Solaize, BP 3, 69360 Solaize, France; corentin.chatelard@orange.fr (C.C.); mathias.dodin@ifpen.fr (M.D.); raquel.martinez-franco@ifpen.fr (R.M.-F.)

⁴ Institut de Recherches sur la Catalyse et l'Environnement de Lyon (IRCELYON), UMR CNRS 5256, Université Lyon 1, 2 Avenue Einstein, 69626 CEDEX Villeurbanne, France; alain.tuel@ircelyon.univ-lyon1.fr

* Correspondence: jean-louis.paillaud@uha.fr

Abstract: Until now, the comprehensive structural analysis of single crystals of zeolite ECR-1, an aluminosilicate with the EON topology, has been hindered owing to the submicron dimensions of the obtained crystals. Additionally, this zeolite, which is characterized by a topology comprising alternating periodic building units of MAZ and MOR layers, exhibits stacking faults that impede accurate refinement through the Rietveld method. In this report, we present, for the first time, the structure of ECR-1 elucidated by studying a nanocrystal with a significantly reduced number of stacking faults. The sample used was synthesized hydrothermally using trioxane as the organic structure-directing agent. The structure determination was conducted using precession electron diffraction (PED) at 103 K. Partial dehydration occurred owing to the high vacuum conditions in the TEM sample chamber. From the dynamical refinement ($R_{obs} = 0.097$), 8.16 Na⁺ compensating cations were localized on six distinct crystallographic sites, along with approximately four water molecules per unit cell. Furthermore, a canonical Monte Carlo computational study was conducted to compare the experimental cationic distribution and location of water molecules with the simulation.

Keywords: nanozeolite; ECR-1; 3D ED; precession; kinematical and dynamical refinement; Monte Carlo simulation



Citation: Örs, T.; Deroche, I.; Chatelard, C.; Dodin, M.; Martinez-Franco, R.; Tuel, A.; Paillaud, J.-L. Determination of Na⁺ Cation Locations in Nanozeolite ECR-1 Using a 3D ED Method. *Symmetry* **2024**, *16*, 477. <https://doi.org/10.3390/sym16040477>

Academic Editors: Partha Pratim Das, Arturo Ponce-Pedraza, Enrico Mugnaioli, Stavros Nicolopoulos and Tomohiro Inagaki

Received: 30 January 2024

Revised: 11 March 2024

Accepted: 28 March 2024

Published: 15 April 2024



Copyright: © 2024 by the authors. Licensee MDPI, Basel, Switzerland. This article is an open access article distributed under the terms and conditions of the Creative Commons Attribution (CC BY) license (<https://creativecommons.org/licenses/by/4.0/>).

1. Introduction

Zeolites, which are microporous aluminosilicate materials, have extensive applications in adsorption, catalysis, and cation exchange for water treatment [1,2]. The overall negative electrical charge of zeolite frameworks allows them to accommodate charge-compensating cations in their pores and cages. The locations and natures of these cations significantly influence their physicochemical properties. For instance, faujasite-type zeolites with FAU topology [3] can be used in various industrial processes, depending on their Si/Al ratios and the nature of the compensating cations [4]. A notable example is lithium-exchanged LSX (Low Silica X), a faujasite with a Si/Al ratio of one, serving as the primary adsorbent for oxygen production from air [5]. Faujasites with higher Si/Al ratios, such as Y zeolites, also play crucial roles as catalysts, with key applications in cracking, isomerization, and hydrocarbon synthesis. In particular, in different enhanced forms, zeolite Y serves as the cracking component in FCC (fluid catalytic cracking) catalysts [6]. Many zeolites with distinct topologies have been synthesized to meet the ever-growing demands of industrial processes. ECR-1, discovered in 1987 [7], is one example. Zeolites with EON topology feature a 2-dimensional pore system defined by straight 12-membered ring (12-MR) channels interconnected through 8-membered ring (8-MR) openings. As illustrated in Figure 1,

this topology can be viewed as a strict alternation of periodic building units (PerBU), namely **MAZ** (PerBU1) and **MOR** (PerBU2) layers. PerBU1 comprises columns along the *a*-axis of *gme* composite building units (CBUs) that are linked to each other via 6-MRs [8]. ECR-1 can be synthesized using various organic structure-directing agents (OSDAs), including bis-(2-hydroxyethyl)- or bis-(2-hydroxypropyl)-dimethylammonium cations [7], adamantane-containing diquateryary alkylammonium iodides [9], and tetramethylammonium [10]. It can even be produced without an organic molecule, thereby reducing production costs [11,12]. ECR-1 has been also produced efficiently via a radicalized seeds-assist route [12]. ECR-1 holds potential applications in the petroleum industry [12] and seawater desalination [13].

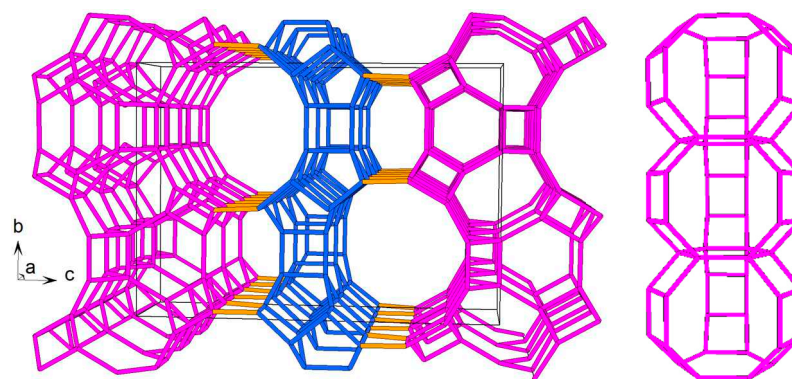


Figure 1. EON topology (left) along the *a*-axis, with PerBU1 and PerBU2 shown in purple and blue, respectively. Perpendicular view (right) illustrates a column formed by stacking three *gme* CBUs. These columns are interconnected through 8-MRs, resulting in the characteristic wavy appearance of PerBU1.

The crystal structure of ECR-1 was initially modeled based on high-resolution transmission electron microscopy (HRTEM) imaging [14]. Subsequent refinement from synchrotron powder diffraction data using the Rietveld method confirmed a structure consisting of alternating mazzite and mordenite layers with a 1:1 stacking sequence ratio [10]. However, variations in synthesis conditions and crystal growth kinetics led to different stacking fault densities. Cation locations were determined during the same Rietveld study [10] conducted on the hydrated form and under ambient conditions. Despite the use of multiple synthesis methods, no structural study from diffraction techniques on single crystal ECR-1 could be carried out owing to the submicron scale of the crystals obtained.

In a recent study, we explored the use of small, six-ring cyclic ether molecules as the organic structure-directing agent (OSDA) to synthesize omega (a synthetic analog of the zeolite mazzite) and ECR-1 zeolites [15]. Notably, 1,3,5-trioxane was employed to synthesize ECR-1. The resulting nanoscale crystals were too small for proper structural analysis from single-crystal X-ray diffraction. Moreover, in the case of ECR-1, diffraction-line broadening owing to the nanosized crystals and overlapping and stacking faults is highly problematic for proper structural analysis using the Rietveld method. For this reason, 3D electron diffraction (3D ED), which is an ensemble of methods in continuous development for the last 20 years, has been proposed for the structural analysis of nanosized single crystals [16]. Indeed, conventional electron diffraction on transmission electron microscopes (TEM) is well established for the characterization of nanoscale materials. However, dynamical scattering observed in electron diffraction does not allow conventional structure analysis to be employed routinely for X-ray diffraction data. To address this, emerging techniques like precession electron diffraction (PED) [17,18], automated diffraction tomography (ADT) [19], rotation electron diffraction (RED) [20], continuous rotation electron diffraction (cRED), and serial rotation electron diffraction (SerialRED) [21] aim to reduce the dynamic effects on observed intensities. Several reviews describe these 3D ED methods and their recent evolutions [21–27]. These methods have proved highly effective in resolving the structures

of many zeolites. They have also been commonly used in combination with X-ray powder diffraction data and/or high-resolution transmission electron microscopy (HRTEM) to elucidate the structure of many zeolitic materials with varying degrees of disorder, such as IM-17, IM-18, MZS-1, zeolite beta, and RUB-5 [28–32].

The objective of the present study was to solve the structure of ECR-1 from a nanosized single crystal (with significantly reduced stacking faults) and to locate the positions of the sodium compensation cations using a 3D ED method (PED), which was chosen owing to its advantages over powder diffraction.

2. Materials and Methods

The ECR-1 of topology EON [3] used in this study was obtained using hydrothermal synthesis following the protocol described by Chatelard et al. [15]. In brief, a gel composed of 10 SiO₂–Al₂O₃–7.5 trioxane–1.7 Na₂O–140 H₂O was stirred at ambient temperature for 3 h before being placed in an autoclave, which was then fixed in an oven equipped with a rotating mechanism for crystallization at 115 °C for 7 days under dynamic conditions (60 rpm). Scanning electron microscopy on the as-synthesized sample showed that the powder was composed of bundles of more or less elongated needle-like crystals of a few hundred nm long and varying diameters [15].

Energy dispersive X-ray spectroscopy (EDX) analysis was performed at a voltage of 15 kV using a JSM-7900F scanning electron microscope (SEM) (JEOL, Tokyo, Japan) equipped with a Quantax analyzer system (BRUKER, Berlin, Germany) made of two XFlash 6-30 detectors. Prior to analysis, the sample was coated with a thin film of carbon using a Baltec SCD004 coater (Balzers, Bal Tec AG, Fürstentum, Lichtenstein).

The high-resolution synchrotron powder-diffraction pattern (SPDP) of the ECR-1 sample was obtained at the ID22 beamline of the ESRF in Grenoble, France [33]. The setup involved a bank of nine scintillation detectors, each preceded by nine Si 111 analyzer crystals, using vertical scanning to measure the diffracted intensity as a function of 2θ , with the channels nominally spaced 2° apart. This Debye–Scherrer capillary geometry configuration guarantees an instrumental contribution to the full width at half-maximum (FWHM) of the diffracted peaks, typically around 0.003° (2θ) in optimal conditions. ECR-1 powder was placed in a thin-walled glass capillary (1 mm in diameter) mounted on a spinner on the axis of the powder diffractometer. A Le Bail refinement [34] was conducted using the free software suite GSAS-II [35].

The PED measurements were conducted using a CM200 TEM (Philips, Eindhoven, The Netherlands) equipped with a DigiStar P2010 (NanoMEGAS, Brussels, Belgium) precession system. Data were recorded by a side entry Phurona CMOS (EMSYS, Münster, Germany) camera (12 M pixel model). An acceleration voltage of 200 kV was applied, and the camera length was set at 1200 mm. A 40 µm condenser aperture and a spot size of 3 were used, and the beam illuminating the sample had a diameter of 105 nm. A Gatan Elsa single-tilt cryo-transfer sample holder was used, enabling data acquisition at a temperature of 103 K. The sample was ground and deposited directly on a carbon-coated Cu grid without prior sonification of the powder in a solvent. In “precession tomography” mode, diffraction patterns were consecutively acquired by manually tilting (without the use of automated acquisition software) the same crystal along the α -axis of the single-tilt cryo-transfer sample holder while precessing the beam. The tilting step size was 1°, and the crystal was rotated in an angular range of –57° to +48°. During rotation, the electron beam was deviated to minimize the exposure time of the sample. Data reduction and integration were performed using PETS2.0 software [36].

We measured 14 crystals, which exhibited different degrees of diffuse scattering in the 00 l direction of the reconstructed sections 0 kl and $h0l$ (data not shown). For the sake of simplicity, results from one crystal, which exhibited a negligible amount of diffuse scattering, will be discussed in the following. The crystal size used for the data collection had dimensions of ~400 × ~200 nm (see Figure S1), rendering it well-suited for the chosen method. During the data-collection process, the electron exposure duration (500 ms per step)

was insufficient to cause observable degradation of the zeolite crystals. As a result, potential disruptions to the quality of the collected data were effectively minimized. The merging was carried out in the Laue class mmm , yielding $R_{int} = 0.1837$ for $n_{obs} = 439$ ($n_{all} = 4428$) reflections. The reconstructed reciprocal-space sections were calculated using PETS2, and sections $hk0$, $0kl$, and $h0l$ are shown in Figure 2a–c. Utilizing the Jana2020 software [37], the structural solution, derived through the charge-flipping algorithm applied to the extracted intensities, directly provided the atomic positions of silicon and oxygen atoms of the ECR-1 framework with EON topology. However, this process required additional steps, including successive difference Fourier map calculations and recycling, to precisely determine the positions of the extra-framework species (compensating Na^+ cations and water molecules). The refinement process included kinematic least-squares refinements on squared amplitudes, denoted as $|F|^2$, and was carried out using the Jana2020 software. To obtain the most accurate model from electron diffraction data, accounting for dynamical diffraction effects, a subsequent dynamical refinement was conducted. In accordance with the dynamical theory of diffraction, the experimentally observed intensities are influenced not only by structural factors but also by the crystal's orientation and thickness. This introduces complexity to the relationship between observed intensities and calculated structural factors. Various parameters must be incorporated during the refinement procedure to account for these effects. The Jana2020 software provides options for dynamical refinement, and the specific details of this method are reported elsewhere [22]. The illustrations of the structures were produced using Vesta [38] or Diamond [39] software.

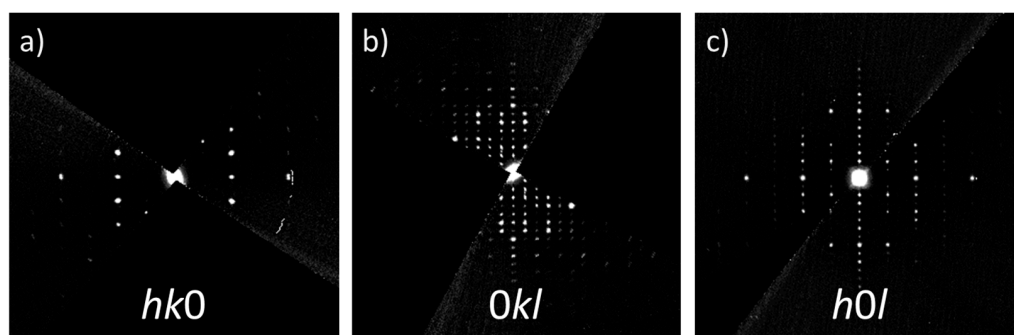


Figure 2. Reconstructed reciprocal-space sections along three different directions (a–c).

In order to investigate the distributions of sodium cations and water molecules throughout various crystallographic sites in the ECR-1 structure, we employed the Monte Carlo (MC) simulation technique using the procedure previously employed for potassium-exchanged faujasite zeolite (KX) [40]. The MC simulations were performed in the canonical ensemble (NVT), where the number of simulated particles N and the simulation cell volume V are kept fixed throughout the simulation, and temperature T is the temperature of the 3D ED experiment (103 K), applying the 8.0.0 version of the Towhee code [41]. The initial microscopic model for the ECR-1 zeolite was derived from the experimental structure with a unit cell chemical composition given by the formula $\text{Na}_{11}\text{Si}_{49}\text{Al}_{11}\text{O}_{120}$ and unit cell parameters of $a = 7.4865 \text{ \AA}$, $b = 17.8463 \text{ \AA}$, and $c = 25.6545 \text{ \AA}$. The aluminum atoms were then distributed according to the Loewenstein rule [42], and various starting Na^+ charge-compensating cation distributions were prepared.

The partial-charge distribution through the atoms of a semi-ionic zeolite structure are given in Table 1. To model the inter-molecular zeolite/zeolite, water/zeolite, and water/water interactions, we employed an expression containing a repulsion–dispersion term and an electrostatic potential term. These contributions were described using the Lennard–Jones (LJ) and Coulombic formulae, respectively. For the ECR-1 zeolite, we extracted the whole set of LJ and Coulombic parameters (q , ϵ , and σ) from the Clay force field [43]. For the water molecule, a five-point potential TIP5P model was employed [44]. In this model, which can reproduce the water liquid density, only oxygen atoms constitute LJ

interaction sites. Moreover, it maintains the molecule rigid with the geometrical parameters set on the experimentally observed values in the gas phase (O–H bond length of 0.9572 Å and HOH angle of 104.52°). Finally, we used the Lorentz–Berthelot combination rules in order to determine the LJ interaction parameters for any pair of unlike atoms.

Table 1. The applied parameters of the Lennard–Jones interaction potential (ϵ , σ) and the partial atomic charges (q) distributed on atoms of adsorbent [43] and adsorbate [44] species.

Parameters for the Non-Bonded Interactions			
Atom	ϵ/k_B (K)	σ (Å)	q (e)
H(H ₂ O)	0	0	0.241
O(H ₂ O)	80.52	3.12	0
L(H ₂ O) (lone pair interaction site)	0	0	−0.241
O (zeolite)	78.20	3.17	−1.094
Si (zeolite)	0.93×10^{-3}	3.30	2.10
Al (zeolite)	0.93×10^{-3}	3.30	1.58
Na ⁺	65.47	2.35	1.00

The simulation box consisted of the unit cell multiplied by four in the x -direction and two in the y -direction (29.9460 Å, 35.6926 Å, and 25.6545 Å) and contained 32 water molecules (corresponding to the experimental loading of 4 H₂O molecules per unit cell). During the MC simulations, the framework atoms (Si, Al, and O) were fixed, whereas the charge-compensating cations and the water molecules were able to displace. An equilibration phase of a Monte Carlo run consisted of 1.0×10^7 steps, while a production phase consisted of 2.0×10^7 steps. The following MC moves were employed: a cation translation and cation intra-box swap move, a water molecule center of mass translation, and a center of mass rotation and water molecule intra-box swap move [41]. The targeted acceptance rate of approximately 50% was maintained by regulating the maximum allowed translations and rotations, which were adjusted during the equilibration phase of the MC run. Periodic boundary conditions were applied in all three spatial directions. Ewald summation was employed to account for Coulombic interactions. Additionally, a cut-off distance of 12.5 Å was considered for Van der Waals interactions.

3. Results and Discussion

As demonstrated in Figure 3, the high-resolution SPDP acquired reveals the existence of trace amounts of nanosized mazzite and mordenite zeolites in the ECR-1 sample. Furthermore, consistent with the findings of Leonowicz and Vaughan [14], our sample displays stacking disorder, as evidenced by the results of the Le Bail refinement (Figure 3).

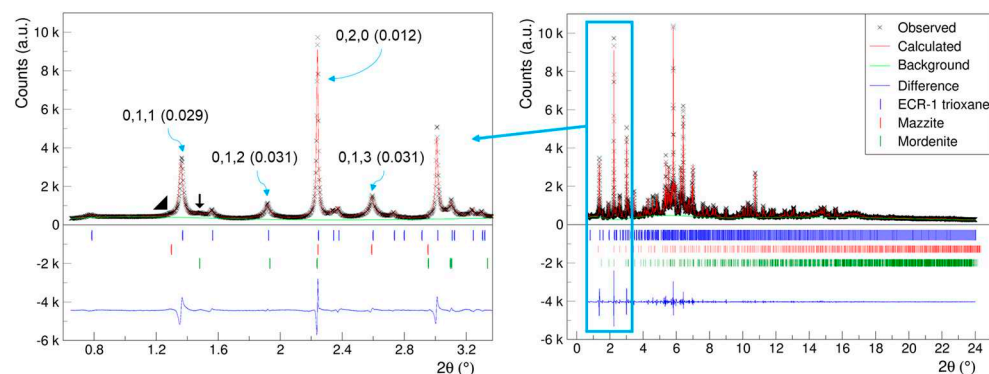


Figure 3. Le Bail refinement plot of ECR-1 ($\lambda = 0.354196$ (3) Å, $a = 7.56159$ (6) Å, $b = 18.1016$ (2) Å, $c = 26.0313$ (4) Å, $wR = 4.8\%$) showing the presence of trace amounts of mazzite (MAZ)▲ and mordenite (MOR)↓ zeolites. The Miller indices are indicated alongside the FWHM values in parentheses for representative reflections.

It is important to highlight that the observed peak broadening is not solely attributable to crystal size/shape effects; rather, there is an anisotropic peak broadening along the *c*-axis, similar to the findings in the structural study conducted by Gualtiri et al. [10]. The FWHM of the reflections showed this marked anisotropy, where reflections with $l \neq 0$ are broad and those with $l = 0$ are sharper. To accurately reproduce the observed powder pattern and account for stacking faults, a DIFFaX [45] simulation is imperative [10] in this case. Accordingly, we conducted a structural study using the 3D ED technique. Our objective was to isolate a nanocrystal with minimal stacking faults, allowing us to directly determine the structure of ECR-1 with EON topology. Furthermore, this approach to structural resolution from single-crystal data provides greater ease in locating compensation cations compared with powder-diffraction methods.

Following kinematical refinement, the final R_{obs} was determined to be 0.1690, and the refined composition was identified as $\text{Na}_{8.84}\text{Si}_{60}\text{O}_{120}$. Additional statistical indicators and refinement parameter details can be found in Table 2. In the kinematical structure refinement, all extra-framework species were refined as compensating cations without considering the presence of water molecules. This oversight was rectified in the dynamical refinement by examining the short Na...Na distances around 2.5 Å and replacing the corresponding sodium atoms with oxygen atoms of water molecules. The post-refinement composition was determined as $(\text{Ow})_{4.52}\text{Na}_{8.16}\text{Si}_{60}\text{O}_{120}$ (where Ow represents the water molecule). Further details regarding the dynamical refinement parameters are shown in the right column of Table 2. The positional parameters, including *x*, *y*, and *z* coordinates, occupancies, and atomic displacement parameters, are provided in Tables S1 and S2 for the kinematical and dynamical refinements, respectively.

Table 2. Crystal and structural refinement data for ECR-1, with two distinct columns highlighting the values that differ between kinematical and dynamical refinements.

	Kinematical Refinement	Dynamical Refinement
Refined empirical formula	$\text{Na}_{8.84}\text{Si}_{60}\text{O}_{120}$	$\text{Na}_{8.16}\text{Si}_{60}\text{O}_{124.52}$
Formula weight	3802.0	3869.5
Temperature/K		103.0
Crystal system		orthorhombic
Space group		<i>Pmnm</i> (#59)
a/Å		7.487 (3)
b/Å		17.846 (12)
c/Å		25.655 (8)
$\alpha = \beta = \gamma / ^\circ$		90
V/Å ³		3427.60 (15)
Z		1
ρ_{calc} g/cm ³	1.842	1.875
F(000)	629.896	635.553
Crystal size/nm		~400 × ~200
Data collection		TEM Philips CM200,
Collection mode		Precession-assisted 3D ED
Source (wavelength)		electrons ($\lambda = 0.02508$ Å)
2 θ range for data collection/ $^\circ$		0.05 to 1.01
Index ranges		$-8 \leq h \leq 9, -23 \leq k \leq 23, -31 \leq l \leq 26$
Reflections collected	4367	17,481
Independent reflections	438 ($R_{\text{int}} = 0.1837$)	1040 (no averaging done)
Data coverage for $\sin\theta/\lambda = 0.6$ Å ⁻¹	92.4%	93%
Data/restraints/constraints/parameters	4367/0/137	17481/17/32/275
Avg./Min/Max crystal thickness	-	526/25/2386 Å
$g_{\text{max}}, R_{\text{sg}}(\text{max})$	-	1.3, 0.5
Goodness-of-fit on F^2	obs: 2.34, all: 1.281	obs: 2.62, all: 0.7976
Final R values [$I \geq 3\sigma(I)$]	$R_{\text{obs}} = 0.169, wR_{2\text{obs}} = 0.358$	$R_{\text{obs}} = 0.097, wR_{2\text{obs}} = 0.1798$
Final R values [all data]	$R_{\text{all}} = 0.604, wR_{2\text{all}} = 0.641$	$R_{\text{all}} = 0.517, wR_{2\text{all}} = 0.2245$

For the treatment of 3D ED data, the persistence of the dynamical effects in kinematical refinement is reflected in the relatively high R values. This phenomenon is commonly observed in electron diffraction techniques, even extending to 3D ED methods, where R_{obs} values of approximately 0.2 or higher are routinely encountered during kinematical

refinements [30,46–48]. However, for the dynamical refinements, the R_{obs} value substantially decreases, reaching as low as 0.097, as shown in Table 2. This fact confirms that high R values obtained during kinematical refinements are mainly due to dynamical effects. Another noteworthy point is the proximity of the atomic scattering factors for Si and Al. This proximity poses a challenge in refining Si and Al positions separately, particularly in the case of mixed tetrahedral site occupancies. Accordingly, in both kinematical and dynamical refinements, all tetrahedral atoms in the framework are refined as Si.

The dynamical refinement method yields superior figures of merit, provides a more comprehensive explanation of the observed electron diffraction intensities, and more accurately represents the crystal structure. As a result, the remainder of the discussion will focus on the outcomes derived from the dynamical refinement process.

As indicated in Table 2, the dynamical refinement results in a composition of $\text{Na}_{8.16}\text{Si}_{60}\text{O}_{124.52}$, where 4.52 oxygen atoms are from adsorbed water molecules. This chemical composition, in terms of sodium content, deviates from the average chemical composition of $\text{Na}_{10.40}\text{Al}_{10.40}\text{Si}_{49.60}\text{O}_{120}$, as determined by EDX (see Figure S2). Approximately 78.5% of the cations are located in the structure, distributed across six distinct crystallographic sites, with occupancies ranging from ~ 0.08 to ~ 0.8 . The disparity between the chemical analysis of the powder and the result of the structural study on an individual nanocrystal can be attributed to the non-uniform distribution of aluminum atoms throughout the sample, potentially altering the number of negative charges within the framework that require compensation.

In a prior study, based on powder XRD data and using the Rietveld method, Gualtieri et al. identified different crystallographic sites for Na^+ in a hydrated zeolite ECR-1 with a similar chemical formula of $\text{Na}_{10.97}\text{Ca}_{0.36}(\text{H}_2\text{O})_x[\text{Al}_{11.54}\text{Si}_{48.46}\text{O}_{120}]$ per unit cell [10]. Figure S3 illustrates the structure refined in this study and that of Gualtieri et al. [10]. The high vacuum conditions in the TEM sample chamber ($\sim 10^{-5}$ Pa) led to partial dehydration, as evidenced by the notable difference in the number of water molecules between the two structures: around 37.5 in the Rietveld study [10] compared with 4.5 in the present structural analysis using 3D ED. In the hydrated state of the ECR-1 sample, the observed weight loss on the thermogravimetric curve after dehydration is approximately 12%, corresponding to roughly 30 water molecules per unit cell [15]. The bond distances between both structures are reported in Table 1Sa in ref. [10] and in Table S3. The average Si—O bond lengths change significantly between the two framework structures, with averages of 1.64 Å in the Rietveld study and 1.61 Å in the current 3D ED study. The O—Si—O angles exhibit similar deformations of the silicon tetrahedrons, where they vary from 95.2° to 122.5° in the Rietveld study and from 101.4° to 122.1° in the present work after dynamical refinement.

Table 3 shows that both crystallographic studies reveal consistent interactions among the compensating Na^+ cations, water molecules, and the framework oxygen atoms. The average shortest distances recorded are 2.58 Å and 2.62 Å in the Rietveld study and the current 3D ED study, respectively. Notably, the Na...O distances exhibit a range, with minimum values of 2.25 Å and 2.29 Å and maximum values of 3.06 Å and 3.08 Å in the former Rietveld and current 3D ED crystallographic studies, respectively.

Table 3. Comparison of Na...O shortest distances after dynamical refinements at 103 K with the Rietveld analysis by Gualtieri et al. [10] at room temperature. Na^+ cations are labeled as C1 to C4.

Gualtieri et al. [10]				This Work			
C1	O13	2×	2.25(4)	Na1	Ow3	2×	2.48(8)
	H ₂ O10	1×	2.36(9)		O22	1×	2.72(4)
	O8	2×	2.36(5)		O10	2×	2.98(2)
	O5	2×	2.95(7)	Na2	Ow2	1×	2.29(2)
	O11	1×	3.03(7)		Ow1	1×	2.32(3)
C2	O11	1×	2.28(4)	O2	2×	2.64(1)	
	H ₂ O1	2×	2.65(2)	O13	1×	2.66(2)	

Table 3. Cont.

		Gualtieri et al. [10]			This Work		
C3	O6	2×	2.76(2)	Na3	O9	1×	2.79(2)
	H ₂ O6	1×	3.06(5)		O16	2×	2.85(2)
	H ₂ O4	1×	2.35(2)		O14	2×	2.41(6)
	H ₂ O5	1×	2.49(4)		O11	2×	2.59(5)
	O20	1×	2.58(3)		O6	1×	2.46(6)
C3b	O14	1×	2.62(3)	Na4	O14	2×	2.52(5)
	O16	1×	2.40(4)		O1	2×	2.57(5)
	H ₂ O4	2×	2.47(4)		Ow2	1×	2.44(1)
C4	O19	2×	2.50(4)	Na5	O13	1×	2.73(1)
	H ₂ O7	1×	2.37(6)		O16	2×	2.83(8)
	H ₂ O3	2×	2.51(4)		O18	2×	3.08(1)
	O22	2×	2.954(4)		O14	2×	2.33(3)
				Na6	O7	1×	2.41(6)
					O11	2×	2.84(4)

However, there is variation in the distribution within the porosity, as depicted in Figure 4. In the hydrated ECR-1, as studied by Gualtieri et al. [10], 67.4% of the cations (C1, C3a, and C3b) are localized in the straight 12MRs channels (Figure 4a).

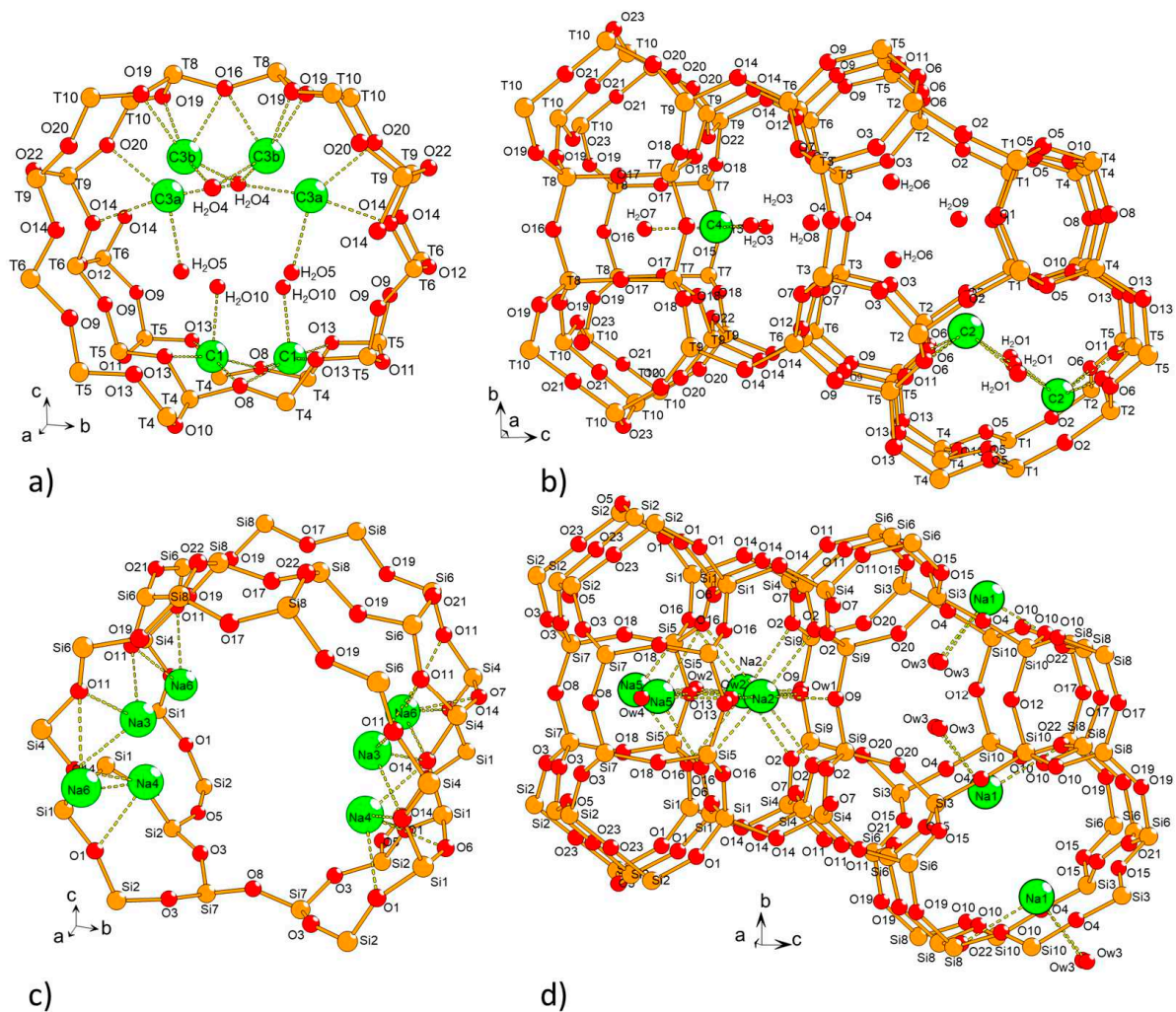


Figure 4. Perspectives showing the cation sites in ECR-1 (a,b) after the Rietveld analysis by Gualtieri et al. [10], where Na⁺ cations are labeled as C1 to C4, and (c,d) from the present crystallographic study using 3D ED. The interatomic distances (Na...O dashed bonds) between the cations and oxygen atoms of the framework, as well as the water molecules, are provided in Table 3.

For the remaining cations, 12.4% are distributed in the 8MRs channels (C4), connecting PerBU1 and PerBU2, and 20.2% within the 8MRs channels (C2) of PerBU2 (Figure 4b). In our present 3D ED study, after partial dehydration, only 32.4% of the cations are located inside the 12MRs (Na3, Na4, and Na6, Figure 4c). The other cations are situated as follows: 4.0% inside the 8MRs opening in PerBU1 (Na5); 38.7% in the 8MRs channels connecting PerBU1 and PerBU2 (Na2) in a site close to C4; and 24.9% within the 8MRs channels of PerBU2 (Na1) (Figure 4d) equivalent to C2. The water molecules remaining after partial dehydration under the vacuum of the TEM are predominantly confined in cavities with openings at 8MRs. This implies an accelerated and facilitated evacuation process when these molecules are situated within the 12MRs channels.

We initially anticipated the presence of trioxane molecules within the pores of ECR-1. Indeed, following the thermogravimetric analysis under air, Chatelard et al. proposed its location in the *gme* composite building units, possibly as a [Na⁺-trioxane] complex [15]. However, Fourier difference maps did not reveal corresponding residual electron densities in the *gme* cage, in the straight 12MRs channels, or elsewhere. This outcome is attributed to the facile evacuation of the neutral trioxane molecules under vacuum. Nevertheless, it is not improbable that the electron beam has induced the reduction of trioxane molecules into carbon monoxide, which can be more readily evacuated through the 8MRs windows of the *gme* units than trioxane itself. Such damage from electron beams on zeolites is frequent, more specifically for the organic part [49].

The averaged cationic distributions of the experimentally determined crystallographic sites in both totally dehydrated and partially hydrated ECR-1 zeolite structures are summarized in Table 4. Comparing the simulated and experimental distributions reveals that cationic site occupancies exhibit similar behavior. Sites Na1 and Na2 are the most populated, followed by sites Na3, Na6, and Na4. In contrast, site Na5, which was unoccupied in the simulation, has the lowest experimental occupancy.

Table 4. Average computed number of charge-compensating Na⁺ cations located proximal to the corresponding experimentally determined crystallographic sites per unit cell.

H ₂ O/Unit Cell		Na1	Na2	Na3	Na4	Na5	Na6	Others
0	Nb. of cations	3.05	2.79	1.50	0.03	0.00	0.49	3.14
	s.o.f. (MC@103 K) ^a	0.76	0.70	0.38	0.01	0.00	0.16	
4	Nb. of cations	2.41	3.00	1.13	0.16	0.00	0.35	3.95
	s.o.f. (MC@103 K) ^a	0.60	0.75	0.28	0.04	0.00	0.09	
	s.o.f. (3D ED) ^b	0.507	0.789	0.212	0.209	0.082	0.240	

^a Site occupancy factors from the canonical Monte Carlo simulation; ^b site occupancies factor from the 3D ED crystallographic study.

Table 5 provides a comprehensive overview of the average distribution of water molecules across various crystallographic sites in ECR-1 zeolite. Despite the non-negligible probability of finding water molecules in the straight 12MRs channels, as depicted in Figure 5, the calculated locations around the cationic sites align well with the experimental trend. While a slight disparity exists between the simulated and experimental cationic distribution and the positioning of water molecules, it is crucial to acknowledge that the Monte Carlo simulation relied on a generic force field. Additionally, the distribution of aluminum atoms within the framework can impact cationic locations. Therefore, given the simplicity of the computational approach, the simulation demonstrates a commendable agreement with the experimental results.

Table 5. Average computed number of water molecules in experimentally determined crystallographic sites.

	Ow1	Ow2	Ow3	Ow4	Na5	Others
Nb. of H ₂ O molecules	0.50	0.38	0.89	0.13	0.32	2.10
s.o.f. (MC-103K) ^a	0.25	0.19	0.11	0.06	0.16	

^a Site occupancy factors from the canonical Monte Carlo simulation.

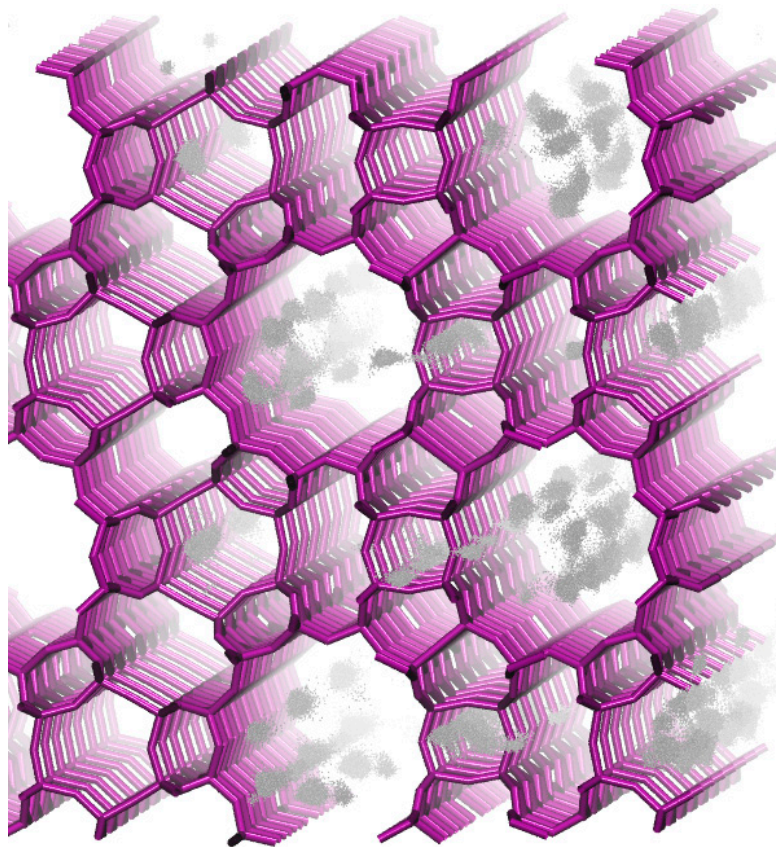


Figure 5. Perspective along the *a*-axis featuring 4000 superposed configurations of H₂O within the simulation box of ECR-1 zeolite at a loading of 4 H₂O per unit cell. Each grey dot corresponds to an oxygen atom of a water molecule.

4. Conclusions

The first structural analysis of ECR-1 zeolite using the 3D ED technique PED has revealed significant insights into its composition, crystal structure, and distribution of charge-compensating cations and water molecules within its framework. The final dynamical refinement ($R_{obs} = 0.097$) led to a chemical composition of Na_{8.16}Si₆₀O_{124.52}, with 4.52 oxygen atoms attributed to adsorbed water molecules. This composition differs from the average chemical composition determined by EDX, indicating a non-uniform distribution of aluminum atoms within the sample. Comparison with a prior Rietveld study highlights the impact of the dehydration phenomenon in the microscope on the crystal structure of ECR-1. The distribution of cations within the ECR-1 framework varies, with the remaining water molecules predominantly confined to cavities that connect 12MRs straight channels. The absence of OSDA trioxane used for the synthesis was attributed to its facile evacuation under the vacuum. However, the possibility of electron beam-induced damage cannot be disregarded. Overall, the experimental findings align well with simulated distributions of cations and water molecules, despite slight disparities that are attributed to the complexity of the framework and computational limitations. The study underscores the importance of advanced structural analysis techniques in elucidating the complex

nature of zeolite frameworks and provides valuable insights for further understanding their properties and potential applications.

Supplementary Materials: The following supporting information can be downloaded at: <https://www.mdpi.com/article/10.3390/sym16040477/s1>, Figure S1: TEM image of the measured ECR-1 crystal. Figure S2: Energy dispersive X-ray spectroscopy (EDX) analyses of ECR-1 zeolite. Figure S3: Projections along the [100] plane of the ECR-1 zeolite (Gualtieri et al. [10] and this 3D ED study, dynamical refinement). Table S1: Fractional atomic coordinates and isotropic displacement parameters (\AA^2) of ECR-1 (3D ED, kinematical refinement). Table S2: Fractional atomic coordinates and isotropic displacement parameters (\AA^2) of ECR-1 (3D ED, dynamical refinement). Table S3: Si-O bond lengths and angles of ECR-1 (3D ED, dynamical refinement), a CIF file, and the corresponding checkCIF file.

Author Contributions: Conceptualization, J.-L.P.; investigation, T.Ö., I.D., C.C., M.D., A.T., R.M.-F. and J.-L.P.; writing—original draft preparation, T.Ö., I.D. and J.-L.P.; writing—review and editing, J.-L.P.; visualization, T.Ö., I.D. and J.-L.P.; supervision, J.-L.P. All authors have read and agreed to the published version of the manuscript.

Funding: This research received no external funding.

Data Availability Statement: CSD 2338838 contains the supplementary crystallographic data for this paper. These data can be obtained free of charge from FIZ Karlsruhe via www.ccdc.cam.ac.uk/structures. (accessed on 8 March 2024).

Acknowledgments: We express our heartfelt gratitude to Pierre Durand of Eloise S.A.S. for his invaluable contributions in adapting the DigiStar P2010 (NanoMEGAS) precession system and his dedicated efforts in maintaining our CM200 microscope. Special thanks go to Loïc Benariac-Doumal, Catherine Dejoie, and Andrew Fitch from ESRF for their invaluable assistance in obtaining the high-resolution powder diffractogram on ID22. Additionally, we extend our appreciation to Laurent Legras, Gatan-EDAX Sales Manager in France, and Ludovic Josien from IS2M for the loan of the single-tilt cryo-transfer sample holder and the EDX measurement, respectively. The authors would like to acknowledge the High-Performance Computing Center of the University of Strasbourg for supporting this work by providing scientific support and access to computing resources.

Conflicts of Interest: The authors declare no conflicts of interest.

References

1. Li, Y.; Li, L.; Yu, J. Applications of zeolites in sustainable chemistry. *Chem* **2017**, *3*, 928–949. [[CrossRef](#)]
2. Li, Y.; Yu, J. Emerging applications of zeolites in catalysis, separation and host–guest assembly. *Nat. Rev. Mater.* **2021**, *6*, 1156–1174. [[CrossRef](#)]
3. Database of Zeolite Structures. Available online: <http://www.iza-structure.org/databases/> (accessed on 15 December 2023).
4. Frising, T.; Leflaive, P. Extraframework cation distributions in X and Y faujasite zeolites: A review. *Microporous Mesoporous Mater.* **2008**, *114*, 27–63. [[CrossRef](#)]
5. Chao, C.C. Process for Separating Nitrogen from Mixtures Thereof with Less Polar Substances. U.S. Patent 4,859,217, 22 August 1989.
6. Vogt, E.T.C.; Weckhuysen, B.M. Fluid catalytic cracking: Recent developments on the grand old lady of zeolite catalysis. *Chem. Soc. Rev.* **2015**, *44*, 7342–7370. [[CrossRef](#)] [[PubMed](#)]
7. Vaughan, D.E.W.; Strohmaier, K.G. Crystalline Zeolite (ECR-1) and Process for Preparing It. U.S. Patent 4,657,748, 14 April 1987.
8. Database of Zeolite Structures—Building Scheme for EON. Available online: <http://www.iza-structure.org/databases/ModelBuilding/EON.pdf> (accessed on 15 December 2023).
9. Hsia Chen, C.S.; Schlenker, J.L.; Wentzek, S.E. Synthesis and characterization of synthetic zeolite ECR-1. *Zeolites* **1996**, *17*, 393–400. [[CrossRef](#)]
10. Gualtieri, A.F.; Ferrari, S.; Galli, E.; Di Renzo, F.; van Beek, W. Rietveld structure refinement of zeolite ECR-1. *Chem. Mater.* **2006**, *18*, 76–84. [[CrossRef](#)]
11. Song, J.; Dai, L.; Ji, Y.; Xiao, F.-S. Organic template free synthesis of aluminosilicate zeolite ECR-1. *Chem. Mater.* **2006**, *18*, 2775–2777. [[CrossRef](#)]
12. Lu, T.; Wang, Z.; Zhang, H.; Qin, J.; Yang, Y.; Cheng, P.; Zhao, Z. Radicalized seeds-assist route for the rapid synthesis of zeolite ECR-1 in the absence of organic templates. *Microporous Mesoporous Mater.* **2022**, *341*, 112071. [[CrossRef](#)]
13. Zhang, Y.J.; Chen, H.; He, P.Y.; Juan Li, C. Developing silica fume-based self-supported ECR-1 zeolite membrane for seawater desalination. *Mater. Lett.* **2019**, *236*, 538–541. [[CrossRef](#)]

14. Leonowicz, M.E.; Vaughan, D.E.W. Proposed synthetic zeolite ECR-1 structure gives a new zeolite framework topology. *Nature* **1987**, *329*, 819–821. [CrossRef]
15. Chatelard, C.; Dodin, M.; Martinez-Franco, R.; Tuel, A. Di- and trioxacyclohexane as structure directing molecules in the synthesis of zeolites omega and ECR-1. *Microporous Mesoporous Mater.* **2021**, *318*, 111015. [CrossRef]
16. Weirich, T.E.; Lábár, J.L.; Zou, X. *Electron Crystallography: Novel Approaches for Structure Determination of Nanosized Materials*; Springer: Dordrecht, The Netherlands, 2006; p. 536.
17. Vincent, R.; Midgley, P.A. Double conical beam-rocking system for measurement of integrated electron diffraction intensities. *Ultramicroscopy* **1994**, *53*, 271–282. [CrossRef]
18. Midgley, P.A.; Eggeman, A.S. Precession electron diffraction—A topical review. *IUCrj* **2015**, *2*, 126–136. [CrossRef] [PubMed]
19. Mugnaioli, E.; Gorelik, T.; Kolb, U. “Ab initio” structure solution from electron diffraction data obtained by a combination of automated diffraction tomography and precession technique. *Ultramicroscopy* **2009**, *109*, 758–765. [CrossRef] [PubMed]
20. Wan, W.; Sun, J.; Su, J.; Hovmoller, S.; Zou, X. Three-dimensional rotation electron diffraction: Software RED for automated data collection and data processing. *J. Appl. Cryst.* **2013**, *46*, 1863–1873. [CrossRef] [PubMed]
21. Wang, B.; Zou, X.; Smeets, S. Automated serial rotation electron diffraction combined with cluster analysis: An efficient multi-crystal workflow for structure determination. *IUCrj* **2019**, *6*, 854–867. [CrossRef] [PubMed]
22. Palatinus, L.; Petříček, V.; Corrêa, C.A. Structure refinement using precession electron diffraction tomography and dynamical diffraction: Theory and implementation. *Acta Crystallogr. Sect. A Found. Adv.* **2015**, *71*, 235–244. [CrossRef]
23. Gemmi, M.; Mugnaioli, E.; Gorelik, T.E.; Kolb, U.; Palatinus, L.; Boullay, P.; Hovmöller, S.; Abrahams, J.P. 3D electron diffraction: The nanocrystallography revolution. *ACS Cent. Sci.* **2019**, *5*, 1315–1329. [CrossRef] [PubMed]
24. Gruene, T.; Mugnaioli, E. 3D electron diffraction for chemical analysis: Instrumentation developments and innovative applications. *Chem. Rev.* **2021**, *121*, 11823–11834. [CrossRef]
25. Samperisi, L.; Zou, X.; Huang, Z. Three-dimensional electron diffraction: A powerful structural characterization technique for crystal engineering. *CrystEngComm* **2022**, *24*, 2719–2728. [CrossRef]
26. Klar, P.B.; Krysiak, Y.; Xu, H.; Steciuk, G.; Cho, J.; Zou, X.; Palatinus, L. Accurate structure models and absolute configuration determination using dynamical effects in continuous-rotation 3D electron diffraction data. *Nat. Chem.* **2023**, *15*, 848–855. [CrossRef]
27. Cho, J.; Willhammar, T.; Zou, X. The synergistic development of electron crystallography and zeolite discovery. *Microporous Mesoporous Mater.* **2023**, *358*, 112400. [CrossRef]
28. Lorgouilloux, Y.; Dodin, M.; Mugnaioli, E.; Marichal, C.; Bats, N.; Caullet, P.; Kolb, U.; Paillaud, J.-L. IM-17: A new zeolitic material, synthesis and structure elucidation from electron diffraction ADT data and Rietveld analysis. *RSC Adv.* **2014**, *4*, 19440–19449. [CrossRef]
29. Cichočka, M.O.; Lorgouilloux, Y.; Smeets, S.; Su, J.; Wan, W.; Caullet, P.; Bats, N.; McCusker, L.B.; Paillaud, J.-L.; Zou, X. Multidimensional disorder in zeolite IM-18 revealed by combining transmission electron microscopy and X-ray powder diffraction analyses. *Cryst. Growth Des.* **2018**, *18*, 2441–2451. [CrossRef]
30. Steciuk, G.; Schäf, O.; Tortet, L.; Pizzala, H.; Hornfeck, W.; Palatinus, L.; Paillaud, J.-L. A new lithium-rich zeolitic 10-MR zincolithosilicate MZS-1 hydrothermally synthesized under high pressure and characterized by 3D electron diffraction. *Eur. J. Inorg. Chem.* **2021**, *2021*, 628–638. [CrossRef]
31. Krysiak, Y.; Barton, B.; Marler, B.; Neder, R.B.; Kolb, U. Ab initio structure determination and quantitative disorder analysis on nanoparticles by electron diffraction tomography. *Acta Crystallogr. Sect. A Found. Adv.* **2018**, *74*, 93–101. [CrossRef]
32. Krysiak, Y.; Marler, B.; Barton, B.; Plana-Ruiz, S.; Gies, H.; Neder, R.B.; Kolb, U. New zeolite-like RUB-5 and its related hydrous layer silicate RUB-6 structurally characterized by electron microscopy. *IUCrj* **2020**, *7*, 522–534. [CrossRef]
33. Fitch, A.; Dejoie, C.; Covacci, E.; Confalonieri, G.; Grendal, O.; Claustre, L.; Guillou, P.; Kieffer, J.; de Nolf, W.; Petitedemange, S.; et al. ID22—The high-resolution powder-diffraction beamline at ESRF. *J. Synchrotron Radiat.* **2023**, *30*, 1003–1012. [CrossRef]
34. Le Bail, A.; Duroy, H.; Fourquet, J.L. Ab-initio structure determination of LiSbWO₆ by X-ray powder diffraction. *Mater. Res. Bull.* **1988**, *23*, 447–452. [CrossRef]
35. Toby, B.H.; Von Dreele, R.B. GSAS-II: The genesis of a modern open-source all purpose crystallography software package. *J. Appl. Cryst.* **2013**, *46*, 544–549. [CrossRef]
36. Palatinus, L.; Brázda, P.; Jelínek, M.; Hrdá, J.; Steciuk, G.; Klementová, M. Specifics of the data processing of precession electron diffraction tomography data and their implementation in the program PETS2.0. *Acta Crystallogr. Sect. B Struct. Sci. Cryst. Eng. Mater.* **2019**, *75*, 512–522. [CrossRef] [PubMed]
37. Petříček, V.; Palatinus, L.; Plášil, J.; Dušek, M. Jana2020—A new version of the crystallographic computing system Jana. *Z. Kristallogr. Cryst. Mater.* **2023**, *238*, 271–282. [CrossRef]
38. Momma, K.; Izumi, F. VESTA 3 for three-dimensional visualization of crystal, volumetric and morphology data. *J. Appl. Cryst.* **2011**, *44*, 1272–1276. [CrossRef]
39. Brandenburg, K.; Putz, H. *Diamond—Crystal and Molecular Structure Visualization*; Version 3.2k4; Crystal Impact: Bonn, Germany, 2018; Available online: <https://www.crystalimpact.de/diamond> (accessed on 3 December 2023).
40. Ammouli, T.; Paillaud, J.-L.; Nouali, H.; Stephan, R.; Hanf, M.-C.; Sonnet, P.; Deroche, I. Insights into water adsorption in potassium-exchanged X-type faujasite zeolite: Molecular simulation and experiment. *J. Phys. Chem. C* **2021**, *125*, 19405–19416. [CrossRef]

41. Martin, M.G. MCCCSTowhee: A tool for Monte Carlo molecular simulation. *Mol. Simul.* **2013**, *39*, 1212–1222. [[CrossRef](#)]
42. Loewenstein, W. The distribution of aluminum in the tetrahedra of silicates and aluminates. *Am. Mineral.* **1954**, *39*, 92–96. Available online: <https://pubs.geoscienceworld.org/msa/ammin/article-abstract/39/1-2/92/539331> (accessed on 21 October 2023).
43. Cygan, R.T.; Liang, J.-J.; Kalinichev, A.G. Molecular models of hydroxide, oxyhydroxide, and clay phases and the development of a general force field. *J. Phys. Chem. B* **2004**, *108*, 1255–1266. [[CrossRef](#)]
44. Mahoney, M.W.; Jorgensen, W.L. A five-site model for liquid water and the reproduction of the density anomaly by rigid, nonpolarizable potential functions. *J. Chem. Phys.* **2000**, *112*, 8910–8922. [[CrossRef](#)]
45. Treacy, M.M.J.; Newsam, J.M.; Deem, M.W.; Treacy, M.M.J.; Newsam, J.M.; Deem, M.W. A General recursion method for calculating diffracted intensities from crystals containing planar faults. *Proc. Math. Phys. Sci.* **1991**, *433*, 499–520. [[CrossRef](#)]
46. Kolb, U.; Gorelik, T.E.; Mugnaioli, E.; Stewart, A. Structural characterization of organics using manual and automated electron diffraction. *Polym. Rev.* **2010**, *50*, 385–409. [[CrossRef](#)]
47. Palatinus, L.; Jacob, D.; Cuvillier, P.; Klementova, M.; Sinkler, W.; Marks, L.D. Structure refinement from precession electron diffraction data. *Acta Crystallogr. Sect. A Found. Cryst.* **2013**, *69*, 171–188. [[CrossRef](#)] [[PubMed](#)]
48. Ge, M.; Wang, Y.; Carraro, F.; Liang, W.; Roostaenia, M.; Siahrostami, S.; Proserpio, D.M.; Doonan, C.; Falcaro, P.; Zheng, H.; et al. High-throughput electron diffraction reveals a hidden novel metal–organic framework for electrocatalysis. *Angew. Chem. Int. Ed.* **2021**, *60*, 11391–11397. [[CrossRef](#)] [[PubMed](#)]
49. Girelli Consolaro, V.; Rouchon, V.; Ersen, O. Electron beam damages in zeolites: A review. *Microporous Mesoporous Mater.* **2024**, *364*, 112835. [[CrossRef](#)]

Disclaimer/Publisher’s Note: The statements, opinions and data contained in all publications are solely those of the individual author(s) and contributor(s) and not of MDPI and/or the editor(s). MDPI and/or the editor(s) disclaim responsibility for any injury to people or property resulting from any ideas, methods, instructions or products referred to in the content.